

PAPER • OPEN ACCESS

Determination of thermally induced effects and design guidelines of optomechanical accelerometers

To cite this article: Qianbo Lu *et al* 2017 *Meas. Sci. Technol.* **28** 115201

View the [article online](#) for updates and enhancements.

You may also like

- [Thermooptics of magnetoactive media: Faraday isolators for high average power lasers](#)
E A Khazanov
- [CaF₂, BaF₂ and SrF₂ crystals' optical anisotropy parameters](#)
I L Snetkov, A I Yakovlev and O V Palashov
- [Novel R-test measurement system to detect thermally induced volumetric accuracy in horizontal machine tools](#)
Lingtao Weng, Dawei Zhang, Weiguo Gao et al.

Determination of thermally induced effects and design guidelines of optomechanical accelerometers

Qianbo Lu[✉], Jian Bai, Kaiwei Wang, Xufen Jiao, Dandan Han, Peiwen Chen, Dong Liu, Yongying Yang and Guoguang Yang

State Key Laboratory of Modern Optical Instrumentation, Zhejiang University, Hangzhou 310027, People's Republic of China

E-mail: wangkaiwei@zju.edu.cn

Received 8 February 2017, revised 1 August 2017

Accepted for publication 7 August 2017

Published 17 October 2017



Abstract

Thermal effects, including thermally induced deformation and warm up time, are ubiquitous problems for sensors, especially for inertial measurement units such as accelerometers. Optomechanical accelerometers, which contain light sources that can be regarded as heat sources, involve a different thermal phenomenon in terms of their specific optical readout, and the phenomenon has not been investigated systematically. This paper proposes a model to evaluate the temperature difference, rise time and thermally induced deformation of optomechanical accelerometers, and then constructs design guidelines which can diminish these thermal effects without compromising other mechanical performances, based on the analysis of the interplay of thermal and mechanical performances. In the model, the irradiation of the micromachined structure of a laser source is considered a dominant factor. The experimental data obtained using a prototype of an optomechanical accelerometer approximately confirm the validity of the model for the rise time and response tendency. Moreover, design guidelines that adopt suspensions with a flat cross-section and a short length are demonstrated with reference to the analysis. The guidelines can reduce the thermally induced deformation and rise time or achieve higher mechanical performances with similar thermal effects, which paves the way for the design of temperature-tolerant and robust, high-performance devices.

Keywords: optomechanics, optical sensing and sensors, microcavity devices, thermally induced deformation, rise time, design guidelines

(Some figures may appear in colour only in the online journal)

1. Introduction

Optomechanical accelerometers are promising candidates for high-performance applications due to their resistance to electromagnetic fields, high resolution and relatively low noise [1–3]. A typical example of the optomechanical accelerometers that we have investigated is shown in figure 1, which

consists of a micromachined elastic sensing structure and an optical cavity-based displacement readout. When the object that the accelerometer is attached to is subjected to an acceleration, the proof mass in the elastic structure moves in the opposite direction relative to the substrate, with a displacement proportional to the acceleration. This leads to a sharp change in the output light intensity since the cavity, composed of a diffraction grating and a high reflective film, is very sensitive to the distance between the grating and the film [4, 5].

Laser-induced effects including light radiation pressure [6] and photothermal effects [7] have received extensive attention



Original content from this work may be used under the terms of the [Creative Commons Attribution 3.0 licence](https://creativecommons.org/licenses/by/3.0/). Any further distribution of this work must maintain attribution to the author(s) and the title of the work, journal citation and DOI.

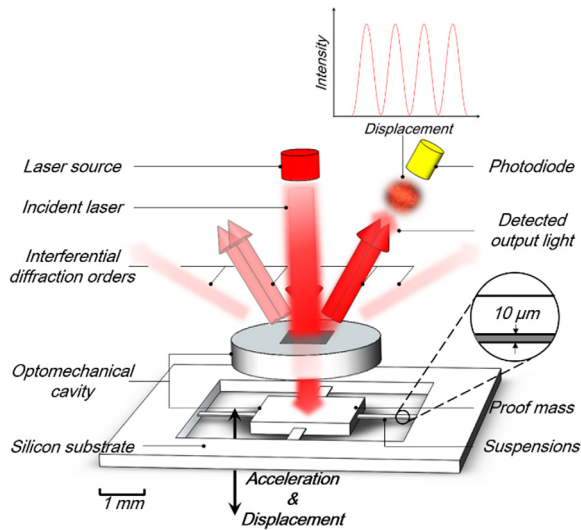


Figure 1. Typical example of an out-of-plane optomechanical accelerometer that is based on an optomechanical cavity.

over recent decades. The radiation force and photothermal phenomena on a nanometer scale have been observed and investigated in the literature and have been used in microactuators [8] and fabrication [9], etc. While at the macroscopic realm, such as in micro-electro-mechanical systems (MEMS) structures with a mass of several milligrams, laser-induced effects, especially thermally induced deformation, have not been studied systematically.

These effects are of great relevance for the performance of sensors and comprise some of the main obstacles for precise measurements that operate over wide temperature ranges, especially for inertial measurement units (IMUs) such as accelerometers [10–12]. An accurate evaluation of the thermal effects of accelerometers, more specifically the deformation and rise time (related to the response speed of the sensor), is critical for realizing reliable and stable devices. There have been many reports that study thermally induced deformation on traditional accelerometers including capacitive [13, 14], resonant [15, 16], and piezoelectric accelerometers [17, 18], among others [19]. Their thermally induced deformation mainly stems from the temperature variation in their operating environments, or the contribution of their electric elements [20–22]. In contrast, the mechanism of the thermal effects of optomechanical accelerometers is very different from the traditional ones, which is attributed to the particular measuring principle. The light sources in optomechanical accelerometers, which can be regarded as heat flux sources, are dominant for the thermal effects, because the mechanical elements are usually passive in typical demonstrations [1–3, 23–25]. The heat flux comes from the proof mass and then propagates to the substrate through the elastic suspensions, which leads to a temperature difference profile of the mechanical sensing element. The temperature profile is changed by the laser irradiation, along with the heat convection with ambient temperature. Then deformation, stress and an unsteady state result. The different geometries and dimensional parameters of the micromachined structure, such as the length, width, and thickness of the suspensions, influence

these thermal effects. It is evident that geometries and dimensional parameters determine the mechanical performances such as sensitivity and resonant frequency. This paper aims to identify the interplay between the mechanical and thermal performances, and thus proposes optimal design guidelines to diminish the thermally induced deformation and rise time without compromising other mechanical performance.

To study the interplay between the mechanical and thermal performances of a specific type of optomechanical accelerometers with a dimension between macro- and micro-scale, both finite-element-analysis (FEA) simulation and analytical calculation are conducted. The laser source is regarded as an input Gaussian heat source, and the heat convection with ambient temperature is also considered. To estimate the rise time, deformation, and output variation, a finite-element model comprising the micromachined elastic sensing structure, adhesive layer and structural support is constructed with thermal loads. We change the geometries and dimensional parameters of the elastic structure to find the relevant rules. A prototype of an optomechanical accelerometer was set up to roughly validate the rules. These variables are adjusted to obtain the optimum balance between the thermal and mechanical performances. The analysis of the thermally induced effects is used in conjunction with the mechanical performances of this device to construct optimized design guidelines. The guidelines aim to reduce the temperature difference, thermally induced deformation, and rise time without compromising mechanical performance, or vice versa, to improve the mechanical performances of the devices with similar thermally induced effects. The analysis and design guidelines may pave the way for temperature-tolerant, high-performance optomechanical devices.

2. FEA modeling

A typical out-of-plane optomechanical accelerometer is illustrated in figure 2(a) [26]. The incident continuous laser beam passes through the diffraction grating and strikes the micromachined sensing structure, which comprises a proof mass, suspension cantilevers and a silicon substrate. It can be regarded as an equivalent heat source with a Gaussian distribution attributed to the light intensity distribution.

The micromachined sensing structure is mounted on a structural support by a heat-conducting glue layer. The heat transfers from the proof mass to the substrate through the suspensions and then to the structural support after passing through the heat-conducting glue layer. There exists a simultaneous heat convection between the ambient environment and the surface of each components.

The laser-induced effects along with the heat convection change the temperature profile of the sensing structure, which leads to the thermally induced deformation. Referring to [27], the scattering force caused by radiation pressure can be neglected because the dimension of the proof mass in our case is large enough compared with atoms or nanoparticles, and the optical power of the incident laser is not very high (~mW). The thermal side effects are ascribed to the heat flux input,

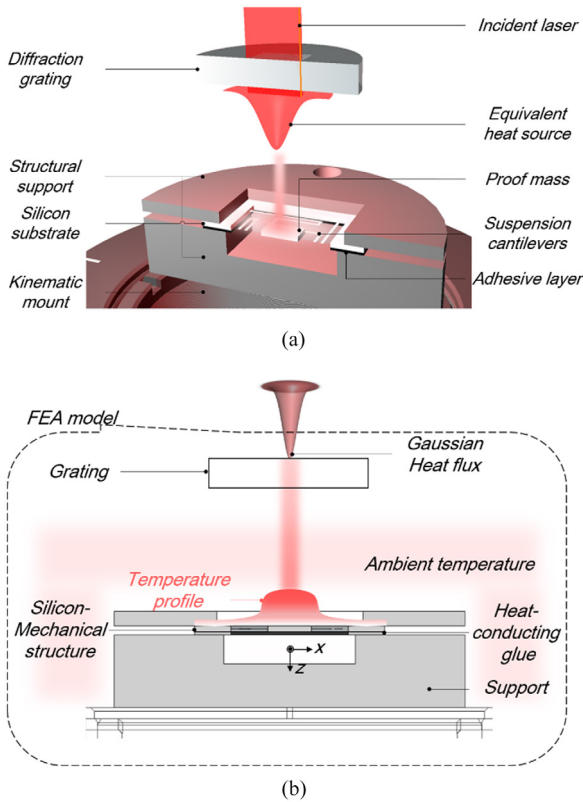


Figure 2. (a) Cross-section schematic diagram of the laser-induced thermal effects of the optomechanical accelerometer. (b) FEA model of the thermal-mechanical dynamic process of the accelerometer.

variable ambient temperature, characterizations of the configuration, and other boundary conditions. It is hard to obtain an analytical solution; hence, we established an FEA model to estimate the temperature profile, rise time, and thermally induced deformation, as shown in figure 2(b). This model is a thermal-mechanical coupling model, which can simulate the mechanical performances of the sensing structure at the same time.

First, the heat source affects the thickness of the grating layer, which changes the cavity length. The grating is made of a quartz slice, whose thickness is 500 μm . According to a simple calculation, the temperature variation caused by laser-induced effects is less than 5 K due to the small absorption coefficient of quartz. Considering the grating's thermal expansion coefficient [28], it can be deduced that the length of the cavity would vary by 1 nm, which is relatively smaller than the variation of the micromachined sensing structure because the sensing structure can be regarded as a micro-displacement amplifier.

In this FEA model, the amplitude of a collimated laser source with Gaussian intensity distribution has the following form along the z -axis [29]:

$$A(r, z) = A_0 \frac{w_0}{w(z)} \exp\left(-\frac{r^2}{w^2(z)} - inz + i\zeta(z)\right), \quad (1)$$

where r is the radial distance from the center axis of the beam, z is the axial distance from the beam's waist, the center of the

Table 1. Important parameters of the FEA model.

Laser power	1 mW
Spot diameter	0.54 mm
Initial ambient temperature	293 K
Thermal conductivity of silicon	149 W $\text{m}^{-1}\cdot\text{K}^{-1}$
Thermal conductivity of adhesive layer	5 W $\text{m}^{-1}\cdot\text{K}^{-1}$
Thermal conductivity of support	237 W $\text{m}^{-1}\cdot\text{K}^{-1}$

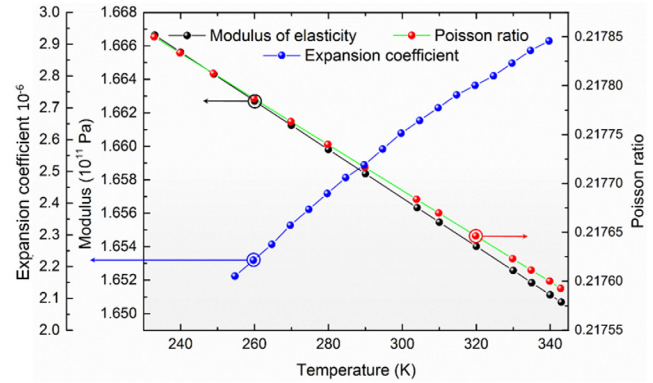


Figure 3. Temperature-dependent parameters of silicon applied in our model. The black line represents the modulus of elasticity, the red line represents the Poisson ratio, and the blue line represents the expansion coefficient.

upper surface of the proof mass is located at the origin point, $w(z)$ is the radius at the axial distance, $w(0)$ is the waist size, or spot diameter of the laser, n is the wave number, and ζ is the Gouy phase shift. Hence, the applied Gaussian heat flux focusing on the upper surface of the proof mass is expressed in the following form:

$$H(r) = \frac{BP_0}{w^2(z)} \exp\left(-\frac{2r^2}{w^2(z)}\right), \quad (2)$$

where P_0 is the initial input light intensity factor of the laser source and B is the absorptivity of power. Although the absorption coefficient of silicon depends on temperature as well [30], it is set to be a constant due to the relatively small laser-induced temperature variation (less than 100 K). The micromachined sensing structures with different dimensional parameters are modeled and meshed via tetrahedral coupled-field solid element SOLID 98 using the commercial software ANSYS, along with the heat-conducting adhesive layer and structural support. We take the thermal conductivity, thermal coefficient of expansion of the materials and the thermal contact resistance into consideration in the analysis. Thermal-structural coupling analysis is chosen to determine the response in the time domain. We begin with an elastic sensing structure with four straight, fixed suspension cantilevers. The initial parameters of the FEA model such as the laser power and spot diameter are included in table 1. The temperature-dependent parameters including the modulus of elasticity, Poisson ratio and expansion coefficient are shown in figure 3, according to the Hall equation [31–33].

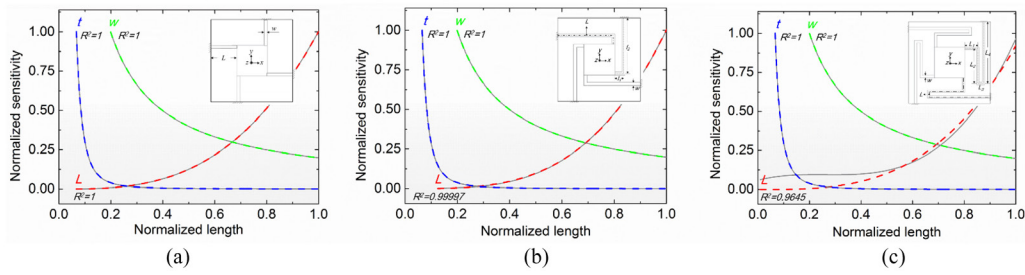


Figure 4. Curve plots of the normalized acceleration-displacement sensitivity versus the dimensional parameters of suspensions such as length, width, and thickness along with their fitted curves for (a) four straight suspensions scheme, (b) crab-leg suspensions scheme, (c) serpentine-leg suspensions scheme, where the gray solid lines represent the calculated values, red dashed lines represent the cubic fitted curves for the length, green dashed lines represent the minus one fitted curves for the width, and blue dashed lines represent the minus 3rd power fitted curves for the thickness.

3. Mechanical performances

Previous studies [34, 35] as well as our prior work [36] have provided paradigms to calculate the mechanical performances of elastic sensing structures including acceleration-displacement sensitivity (marked as s_{a-d}), resonant frequency, and stress profile.

More precisely, for an elastic structure with four straight suspensions, s_{a-d} can be expressed as [34]

$$s_{a-d\text{straight}} = \frac{mL^3}{4Ewt^3}, \quad (3)$$

where m is the mass of the proof mass; L , w , and t are the length, width, and thickness of suspensions, respectively; and E denotes Young's modulus of the material. It is obvious that L and t have more considerable effects on sensitivity because sensitivity is proportional to the cube of L and inversely proportional to the cube of t but is only inversely proportional to w . For crab-leg and serpentine-leg flexure, or other geometries (such as folded flexure), although the specific expressions are somewhat different, the tendencies are similar, as shown in figure 4 and expressed as follows [26]:

$$s_{a-d\text{crab}} = \frac{m}{4} \left(\frac{N_0^2 l_1 + l_1^3 / 3 - N_0 l_1^2}{S_e} + \frac{U_0^2 l_2 + l_2^3 / 3 - U_0 l_2^2}{S_e} + \frac{(N_0 - l_1)^2 l_2}{S_g} \right). \quad (4)$$

$s_{a-d\text{serpentine}}$

$$= \frac{m}{8S_e} \left[\begin{array}{l} N_1 L_1^2 - U_1 L_2^2 + 2N_1 L_1 L_3 \\ -N_1 L_3^2 - 2U_1 L_2 L_4 + U_1 L_4^2 \\ + \frac{2(L_1^3 + L_2^3 + L_3^3 + L_4^3)}{3} \\ + 2L_1 L_3 (L_1 - L_3) + 2L_2 L_4 (L_2 - L_4) \end{array} \right] + \frac{m}{4S_g} \left[\begin{array}{l} N_1 L_1 L_2 - U_1 L_2 L_3 + N_1 (L_1 + L_3) L_4 \\ + L_1^2 L_2 + L_2^2 L_3 + (L_1 + L_3)^2 L_4 \end{array} \right]. \quad (5)$$

Herein $S_e = EI_x$, $S_g = GJ$, $J \approx t^3 w / 3$, and G denotes the shear modulus of elasticity. Parameters N_0 , N_1 and U_0 , U_1 are defined by

$$N_0 = \frac{l_1^2 S_g + 2l_1 l_2 S_e}{2(l_1 S_g + l_2 S_e)}, U_0 = \frac{l_2^2 S_g}{2(l_1 S_e + l_2 S_g)}, \quad (6)$$

$$N_1 = \frac{S_g(L_3^2 - L_1^2 - 2L_1 L_3) - 2S_e(L_1 L_2 + L_1 L_4 + L_3 L_4)}{2S_g(L_1 + L_3) + 2S_e(L_2 + L_4)} \quad (7)$$

$$U_1 = \frac{S_g(L_2^2 - L_4^2 + 2L_2 L_4) + 2S_e L_2 L_3}{2S_g(L_2 + L_4) + 2S_e(L_1 + L_3)},$$

in which $L = l_1 + l_2$, and $L = L_1 + L_2 + L_3 + L_4$ in two geometries.

In regard to other types of performances, namely the resonant frequency and maximum stress in the structure, we can estimate them using FEA and theoretical approaches, as well. The 1st resonant frequency is defined as

$$\omega = \sqrt{\frac{k}{m}} = \frac{1}{2} \sqrt{\frac{1}{s_{a-d}}}, \quad (8)$$

where k is the spring constant. Compared with the sensitivity (s_{a-d}), the resonant frequency changes relatively slowly with the dimensional parameters of the suspensions. More specifically, the resonant frequency has a minus 3/2 power regularity over the length, plus 3/2 power regularity over the thickness and a 1/2 power regularity over the width. According to the simulation [37], it can easily be found that the improvement in sensitivity hardly affects the maximum stress.

In conclusion, for an out-of-plane mechanical sensing structure, different dimensional parameters of the suspensions have different weight factors on the impact of mechanical performances. The length and thickness influence the mechanical performances more significantly than the width. Therefore, they can be tailored for different aims.

4. Thermally induced effects

In this section we investigate thermally induced effects, and try to identify the interplay between the mechanical performances and thermally induced effects. The variables include the laser power and spot diameter, the dimensional parameters of the suspensions and their geometries, as well as the ambient temperature. The evaluated parameters include the temperature profile, rise time, and thermally induced deformation. The temperature profile in terms of the laser irradiation, which subsequently causes thermally induced deformation, would finally affect the length of the cavity and the output. We obtain the partial derivatives of the curves of the temperature

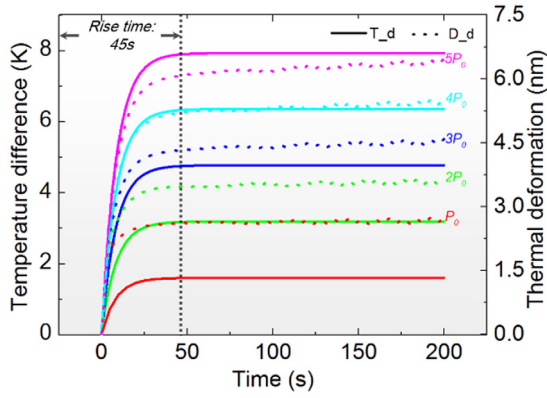


Figure 5. Temperature difference and thermally induced deformation versus the irradiation time for different laser power. The temperature differences are shown as solid curves, marked as T_d , and the thermally induced deformation are spot curves, marked as D_d .

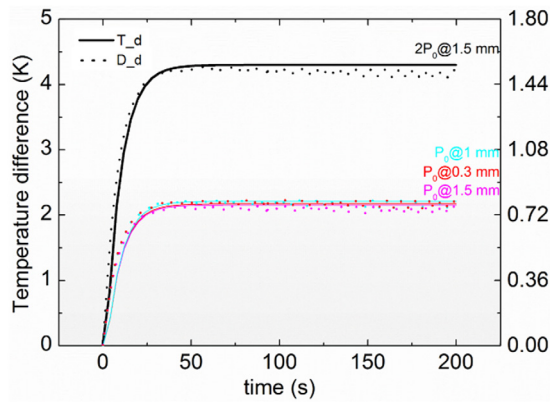


Figure 6. Temperature difference and thermally induced deformation versus irradiation time for different laser spot diameters with the same power. The temperature differences are shown as solid curves, marked as T_d , and the thermally induced deformation are spot curves, marked as D_d .

difference versus irradiation time and define the rise time by the point whose derivative is equal to 0.0025.

4.1. Laser influence

Figure 5 depicts the simulated responses including the temperature difference and thermally induced deformation versus the irradiation time when the laser power increases from P_0 to $5P_0$. According to the simulation, the temperature difference between the center of the proof mass and substrate and the out-of-plane displacement of the proof mass (thermally induced deformation) are found to be proportional to the power, that is, to the input heat flux. Furthermore, it is obvious that the power of the incident laser is irrelevant for the rise time.

To estimate the impact of the spot diameter of the laser, the overall heat flux should be identical, which can be described using the following equation:

$$\begin{aligned} H_{w_1} &= \frac{BP_1}{w_1^2} \int_0^\infty \exp\left(-\frac{2r^2}{w_1^2}\right) \cdot 2\pi r dr \\ &= H_{w_2} = \frac{BP_2}{w_2^2} \int_0^\infty \exp\left(-\frac{2r^2}{w_2^2}\right) \cdot 2\pi r dr, \end{aligned} \quad (9)$$

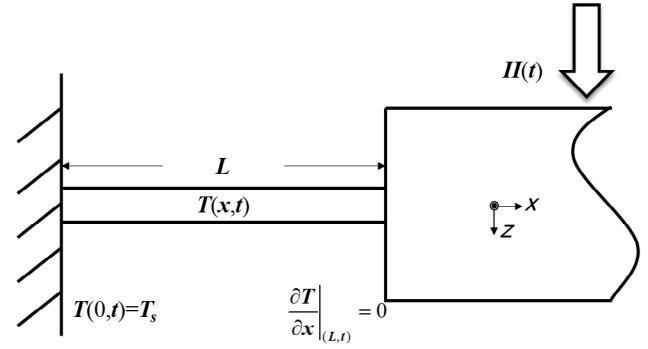


Figure 7. Schematic of the simplified sensing structure subjected to a periodic heat source.

where w_1 and w_2 are the spot diameters of the laser, and P_1 and P_2 are the corresponding power factors.

As depicted in figure 6, the spot diameter has a negligible impact on the thermally induced effects if the incident laser power is identical to P_0 . The small deviation in the simulation results of the different sets of the spot diameter is mainly attributed to the insufficient mesh number in terms of the small irradiation area.

A mechanical structure can be excited thermally via ballistic heating [38–40]; thus, it is worthwhile to discuss the thermal resonance under laser excitation.

To qualitatively describe the resonance phenomenon, our structure is simplified to a 1D case, as shown in figure 7. Because the substrate and the bulk proof mass are far larger than the micro suspensions, they can be regarded as two isothermal objects. Hence the boundary conditions can be described as

$$\begin{aligned} T(0, t) &= T_s \\ \frac{\partial T}{\partial x} \Big|_{(L, t)} &= 0, \end{aligned} \quad (10)$$

where $T(x, t)$ is the temperature function of the spatial and temporal values. According to the Cattaneo–Vernotte hyperbolic heat conduction model [41], the conditions that can excite thermal resonance can be deduced:

$$\alpha \nabla^2 T + \frac{1}{\rho c_p} \left[H + \frac{\alpha}{C^2} \frac{\partial H}{\partial t} \right] = \frac{\alpha}{C^2} \left(\frac{\partial}{\partial t} + \frac{\partial^2}{\partial r^2} \right) T(x, t). \quad (11)$$

Herein C is the thermal wave speed, α is the thermal diffusivity, ρ is the density of the material, c_p is the heat capacity, and the function of the heat source has the following form:

$$H(t) = q \exp(i\Omega t), \quad (12)$$

in which Ω denotes the oscillation frequency of the applied heat source. The frequency of the heat source should be larger than $\sqrt{\sqrt{2} - 1}f$ to produce the thermal resonance, while f is the critical frequency of the material, which is the reciprocal of the relaxation time τ (1.1×10^{-8} s for silicon). If the applied frequency is larger than this critical value, the excitable mode number of the thermal wave can be obtained:

$$n \geq 0.6436 \frac{L}{\pi C \tau} \simeq 0.6436 \frac{L}{\pi \alpha} \quad (13)$$

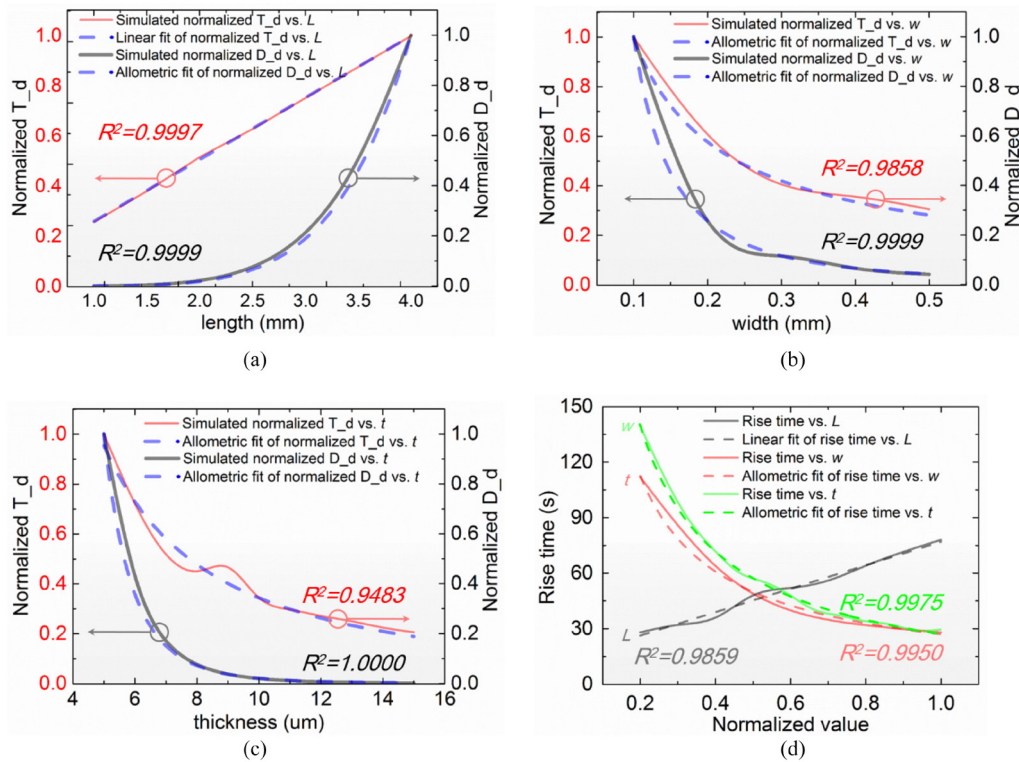


Figure 8. Curves of the normalized temperature difference and thermally induced deformation versus (a) length, (b) width, and (c) thickness with fitted curves. (d) Curves of the rise time versus normalized value of length, width and thickness with fitted curves. Simulated curves are presented as solid lines, and the allometric fittings are presented as dashed lines. The temperature difference and rise time are directly proportional to the length but inversely proportional to the width and thickness. The thermally induced deformation is proportional to the minus second power of the width, while plus and minus third power is proportional to the length and thickness, respectively.

by substituting the length of the suspension and the thermal diffusivity for silicon ($9.4 \times 10^{-5} \text{ m}^2 \text{ s}^{-1}$). The critical mode number for the thermal resonance is approximately five, which means that five thermal modes can occur if the thermal wave can be excited. Furthermore, it is found that the thermal resonance that is produced by a periodic heat source does not transport energy, which can be derived by both parabolic and hyperbolic equations [42].

However, the laser source we adopted is a continuous laser. The laser frequency, which is on the order of 10^{15} Hz (for a He-Ne laser with a 632.8 nm wavelength, the frequency is 4.74×10^{14} Hz), is much higher than the critical frequency of the excited heat source ($\sim 9 \times 10^7$ Hz). Thus, the thermal resonance in terms of the laser frequency can be neglected, which means that a continuous laser cannot excite thermal resonance. A periodic chirp laser with an appropriate frequency can be implemented to investigate the phenomenon. However, it is beneficial to use a continuous laser for the accelerometer to avoid the thermal resonance, which may lead to an additional dynamic displacement.

4.2. Dimensions and geometries of suspensions

The dimensional parameters of the suspension cantilevers also influence the thermally induced effects. The factors considered for the suspensions are as follows: length, width, thickness and geometry. To simplify the discussion, dimensions of the proof mass and silicon substrate as well as other

parameters remain unchanged. Simulated thermal responses versus the variable dimensions are performed, as shown in figure 8. As shown in figures 8(a) and (d), the temperature difference and rise time have a good linear relationship with the length of the suspensions. In addition, the temperature difference and rise time are inversely related to the width and thickness, as shown in figures 8(b)–(d). The simulated curves are in excellent agreement with those fitted linear or inverse ratio curves (dashed lines), as demonstrated by the coefficient of determination, R^2 , embedded in figure 8.

It is interesting to find that the dynamic thermal responses can be characterized by the thermal-conductivity-independent thermal resistance for this specific metric. We term the shape factor as $CSF = L/S$, which is defined by a quotient of the length L and a cross-sectional area $S = w \times t$. Actually, the thermal resistance is derived from Fourier’s law of heat conduction, which assumes an infinite heat propagation velocity. It may not be suitable for this thermodynamic process, but fortunately the parabolic heat conduction equation can describe the heat transfer phenomena in our sensing structure well.

In our case, figure 9(a) indicates that the simulated thermal responses roughly scale as CSF increases. While for the suspensions with different dimensions but the same CSF (CSF_1), it is evident that the thermal responses are nearly identical compared with those with different CSF (CSF_2), as shown in figure 9(b). This factor is found to be able to characterize the thermal effects effectively, especially the temperature

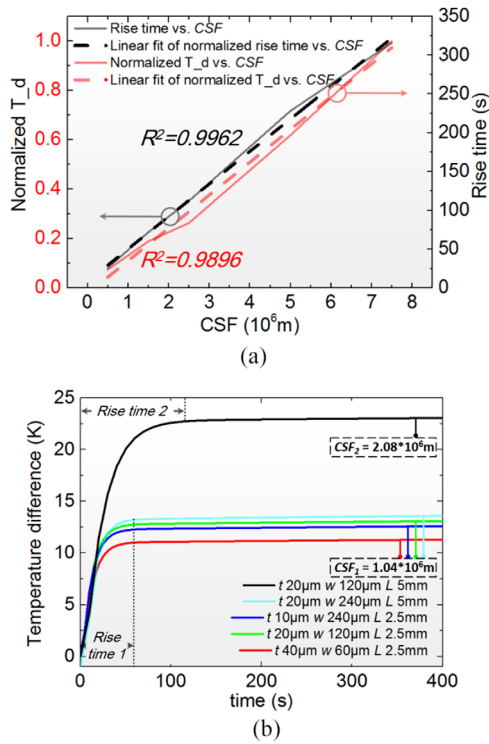


Figure 9. (a) Curves of the normalized temperature difference and rise time versus CSF with their linear fitted curves. The solid lines are the simulated curves, and dashed lines are the fitted ones. (b) Thermal response versus irradiation time with the two typical CSF and different dimensional parameters.

difference and rise time. While for the thermally induced deformation, as sketched in figures 8(a)–(c), the trend differs since it is relevant to the stiffness of the structure and the temperature profile of the suspensions. Combined with the temperature profile, the trend of the thermally induced deformation is slightly different from the mechanical performances without considering the heat flux input. According to the allometric fits of the curves, the tendencies of the thermally induced deformation as a function of length and thickness are similar to the mechanical sensitivity versus length and thickness (approximately plus or minus third-order relation), but more sensitive to the decrease in width compared with the mechanical sensitivity (minus second power versus inversely proportional relationship).

Preceding simulations are based upon observations on an elastic sensing structure with four straight, fixed suspension cantilevers, but the phenomenon is not confined to the straight cantilevers. When the geometry changes, it is found that the aforementioned laws still hold if the cross-section is consistent. We set up two other geometries, as shown in figures 3(b) and (c). As a comparison, the factor CSF of the crab-leg and serpentine-leg suspensions is set to be the same as the straight one. Three sets of temperature profiles and rise time are almost identical, as shown in figure 10. When the CSF of these two geometries changes, the temperature difference and rise time vary almost linearly with the factor, as verified by the parameter ‘CSF/temperature difference’, listed in table 2.

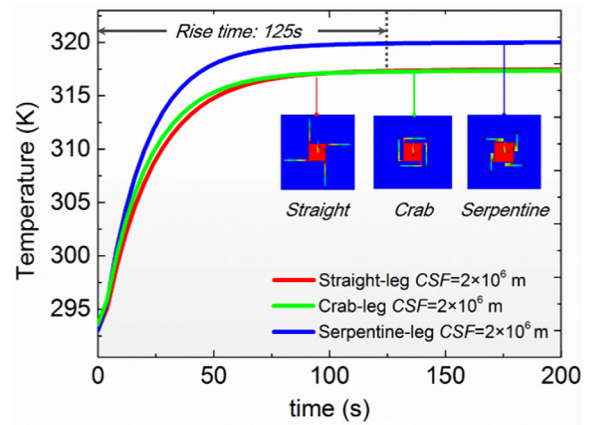


Figure 10. Thermal responses versus irradiation time of different geometries with the same CSF. The responses and tendencies of three sets with the same CSF are almost the same. Although there is a slight deviation between the serpentine-leg set and others, the deviation is far smaller than that with different CSF, as shown in figure 9(b).

4.3. Natural convection with ambient temperature

In the FEA model, the heat convection with ambient temperature is also taken into consideration. The sensing structure is irradiated at the beginning in stage 1. Then, the ambient temperature is adjusted from room temperature (293 K) to 313 K after the system is stable, with a rise of 20 K in stage 2; after that, the ambient temperature is adjusted to the room temperature in stage 3. Figure 11 illustrates the thermal response during the three stages. This indicates that the response attributed to the natural convection with ambient temperature is far slower than that in terms of laser irradiation or internal temperature change. However, the induced deformation, represented by the blue dashed-dot line, cannot be ignored although the variation in the temperature difference between the proof mass and substrate is small. This is mainly because the support in our case is much thicker and larger (~cm) than the micromachined sensing structure. The thermal expansion of the support and the thermodynamic convection process is much slower.

To sum up, the impact of heat convection with ambient temperature depends on the dimensions of the support and the substrate. The larger the support compared with the sensing structure, the slower and larger the response is compared with that due to laser irradiation.

4.4. Rough empirical evidence

The thermal responses of the optomechanical accelerometer were observed by establishing a prototype, as shown in figure 12. The sensing structures (proof mass: 8.7×10^{-6} kg) with serpentine-leg suspensions (set 1: overall length 12 mm, width 0.24 mm, thickness 10 μm, CSF 5×10^6 m) and crab-leg suspensions (set 2: overall length 6.35 mm, width 0.3 mm, thickness 10 μm, CSF 2.12×10^6 m) were assembled with a diffraction grating to construct an optomechanical cavity, and this cavity was fixed on a structural support using a heat-conducting glue. This cavity was rigidly mounted on a high-precision rotation stage, together with the laser source (Model

Table 2. Thermal responses of different geometries with different CSF.

Geometries and CSF	Dimensional parameters	Temperature difference (K)	Rise time (s)	CSF/temperature difference (10^4 m K^{-1})
Straight $0.83 \times 10^6 \text{ m}$	$2.5 \text{ mm} \times 300 \mu\text{m} \times 10 \mu\text{m}$	12.23	72	6.79
Crab $2.12 \times 10^6 \text{ m}$	$(1 + 5.35) \text{ mm} \times 300 \mu\text{m} \times 10 \mu\text{m}$	35.99	150	5.89
Serpentine $4.80 \times 10^6 \text{ m}$	$(1.28 + 3.42 + 0.8 + 6.02) \text{ mm} \times 240 \mu\text{m} \times 10 \mu\text{m}$	77.52	333	6.19

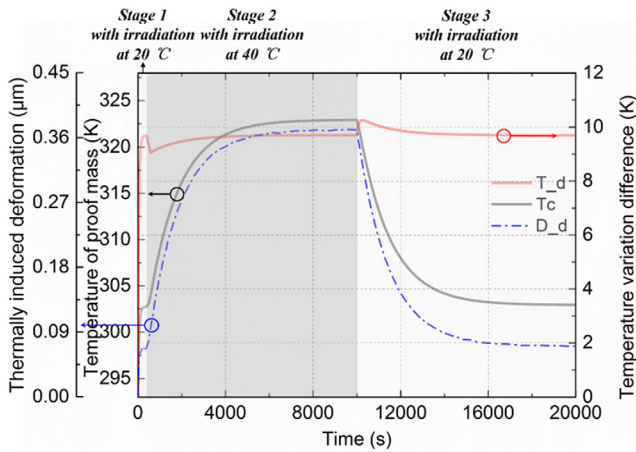


Figure 11. Thermal responses versus time during irradiation and natural convection when ambient temperature changes. The ambient temperature is adjusted from 293 K to 313 K at 400 s, then returns to 293 K at 10000 s. The temperature of the proof mass, temperature difference and deformation are represented by the red, grey and blue line, respectively.

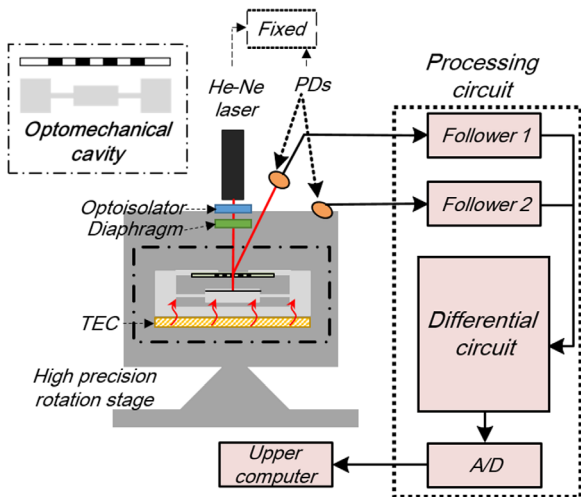


Figure 12. Prototype of the optomechanical accelerometer for the static test. Two photodiodes along with two followers and a differential circuit are employed to realize differential measurement using an ambient light.

05-STP-912, Melles Griot Inc.), two photodiodes (Model S8745-01, Hamamatsu Inc.), a precise kinematic mount and a processing circuit. To diminish the influence of backward laser, an optoisolator comprising a polaroid and a half-wave plate was employed. An adjustable diaphragm was introduced to control the laser turning on or off. The wavelength of the

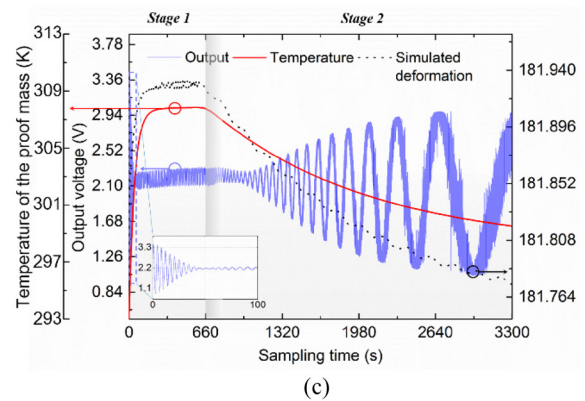
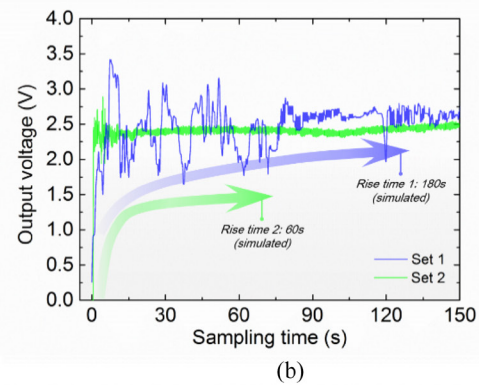
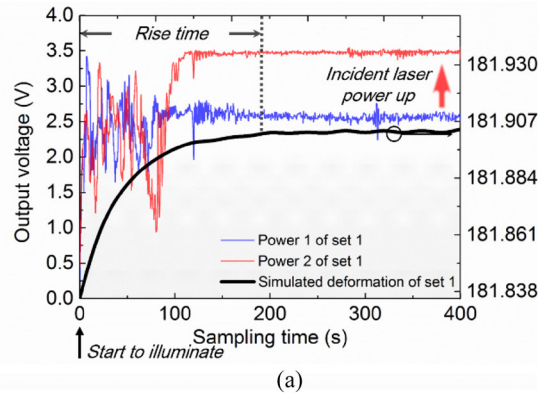


Figure 13. Output voltage of the prototype versus sampling time along with the laser power change. (a) Output of set 1 when the incident laser power changes; the blue line is at low power, the red line represents higher power, and the black line is the simulation result. (b) Output curves of set 1 and its comparison with set 2; the green line represents set 2. (c) Output of set 1 in two stages along with the measured temperature and the simulated deformation; the sensing structure was heated to a specific temperature in stage 1, while it cooled via natural convection with ambient temperature in stage 2.

Table 3. Interplay of the mechanical performances and thermally induced effects for an out-of-plane sensing structure.

Evaluation parameters/variables	Sensitivity _{a-d}	Max stress	Resonant frequency	Temperature difference	Rise time	Thermally induced deformation
Laser spot diameter	N/A	N/A	N/A	→	→	→
Laser power	N/A	N/A	N/A	↗	→	↗
Length	↗↗↗	→	↘(3/2)	↗	↗	↗↗↗
Width	↘	↘	↗(1/2)	↘	↘	↘↘
Thickness	↘↘↘	↘↘	↗(3/2)	↘	↘	↘↘↘
Ambient temperature	N/A	N/A	N/A	↗	→(much longer)	↗

→ : irrelevant, ↗: positive correlation, ↗↗↗: positive three-power relation, ↘: inversely proportional relation, ↘↘: inverse square relation, ↘↘↘: inverse three-power relation.

Table 4. Performances of different sensing structures with different dimensions.

Dimensions of suspensions (thickness × width × length)	CSF (10 ⁶ m)	Sensitivity _{a-d} (μm g ⁻¹)	Max stress (MPa per 1 g)	Resonant frequency (Hz)	Temperature difference (K)	Rise time (s)	Thermally induced deformation (nm)
5 μm × 480 μm × 1.58 mm (Optimal)	0.66	8.16	37.83	174.54	6.68	45	0.83
8 μm × 240 μm × 2 mm	1.04	8.21	27.19	174.21	12.01	72	2.62
10 μm × 240 μm × 2.5 mm	1.04	8.23	21.66	173.93	12.23	72	5.27
20 μm × 120 μm × 2.5 mm	1.04	2.08	18.58	346.42	12.73	72	5.63
40 μm × 60 μm × 2.5 mm	1.04	0.52	18.21	689.65	10.97	71	5.61

incident laser was 632.8nm, and two photodiodes with a responsivity of 0.33 V nW⁻¹ were adopted to achieve differential measurement with ambient light [43]. Furthermore, a thermal electrical refrigerator (TEC) was adhered to the optomechanical cavity to adjust the temperature of the sensing structure.

The real-time responses of two prototypes were recorded when the tilt angle of the rotation stage was invariant, which means that the applied acceleration is certain. Herein the acceleration is 9.8 m s⁻² in terms of the vertical direction of gravity.

The output voltages versus measurement time are presented in figure 13. As marked in this figure, when the sensing structure was irradiated, the output voltage of the prototype instantly began to vary. For set 1, this system gradually entered a steady state after approximately 200s. With respect to the thermally induced deformation curve of the serpentine-leg structure when subjected to 1 unit of gravity (blue line in figure 13(a)), the tendency and rise time match well with the simulation result, which is shown as the bold black curve in figure 13(a). There exists a violent oscillation in the experimental result. This is mainly due to the ultra-high sensitivity of acceleration and phase ambiguity in the interferometry detection. Small vibrations, air turbulence, or even a switching of an optoisolator affect the responses. The influence factors are hard to separate. Then, we changed the incident laser power by rotating the polaroid, which is shown as the red line in figure 13(a). The tendency and rise time were consistent with the former conditions, while the stable output had a bias. This demonstrates that the rise time is not concerned with the incident laser power (heat flux).

Figure 13(b) indicates that set 2 can be stabilized faster than set 1. The rise times of set 1 and set 2 are 60s and 180s, respectively, according to the simulation.

Figure 13(c) shows the thermal responses in different stages. Stage 1, which is the overall sensing structure along with the support, was heated from 299 K to approximately 309 K and held for 660s; the sensing structure was cooled via natural convection with ambient temperature in stage 2, corresponding to stage 3 in figure 11. The room temperature was 299 K, and heating was carried out via both laser irradiation and TEC. Because the connection of components is not a rigid coupling and the thermal expansion is not uniform, the contrast ratio changes with the temperature variation [34]. However, the overall deformation can be obtained via the number of the period of the output. The tendencies of the measured temperature (red solid line) and the output voltage (blue solid line) match well, as well as the simulated deformation, which indicates that the heat convection with ambient temperature has a far slower response than that due to irradiation and TEC. Although there are deviations in the experimental and simulation results, the tendencies are correct. The deviation between the obtained deformation and simulation result is mainly because our prototype setup was not integrated; the thermal expansion of the kinematic mount and even the rotation stage contributed to the huge deformation.

Because it is hard to obtain the temperature profile of this extremely brittle MEMS structure, we estimate the temperature response via the thermally induced deformation or output voltage. In the future, a micro thermocouple can be integrated in the sensing structure to detect the temperature profile.

Although the experimental results are not perfect due to large oscillation and phase ambiguity, the empirical evidence qualitatively confirms the validity of our transient model, which can predict the thermal response, including thermally induced deformation and rise time. The tendency and laws predicted by the model are critical.

5. Design guidelines for high performance

Based on the aforementioned analysis, optimized design guidelines will be proposed in this section, combined with the mechanical performances and thermally induced effects. This aims to diminish the thermally induced deformation and rise time without compromising mechanical performances, or to realize higher performances with the same thermal effects.

We give a short overview of the relation between the relevant factors and thermal effects, as well as other mechanical properties, as listed in table 3.

For the mechanical performances, the width carries less weight than the length and thickness, especially for the sensitivity. However, for the thermal effects, there is an increased importance for the width. Specifically, the length, width, and thickness are three equally important parameters for the temperature difference and rise time. For the thermally induced deformation, the importance of the width also increases. To tailor the mechanical performances along with the thermally induced deformation and rise time, the width of the suspensions can be fully taken advantage of.

Optimized design guidelines for an out-of-plane sensing structure can be induced from the discussion. To reduce thermally induced deformation and rise time under the premise that the out-of-plane sensitivity is still high, adopting suspensions with a flat cross-section (large width and small thickness) and a short length is appropriate. For the pursuit of higher sensitivity without expense of larger thermal effects, the width can be further increased while the thickness and the length can be decreased to the same extent, as long as CSF stays the same. Notably, the large width is the key point in optimized design guidelines.

Table 4 shows the thermal responses and mechanical performances with different dimensions of the suspensions. It is demonstrated that higher mechanical performances with similar thermal effects or smaller thermal effects with the same mechanical performances can be realized by applying these design guidelines.

These guidelines are of great significance for designing a single-axis, temperature-tolerant, high-performance optomechanical accelerometer, which commonly contains an elastic sensing structure and a laser-induced heat source.

6. Conclusion

This paper systematically investigates the thermal effects of a single-axis optomechanical accelerometer, especially the laser-induced effects. The temperature difference, rise time and thermally induced deformation are evaluated via FEA modelling and then characterized using a thermal resistivity-related length dimension parameter *CSF*. The rise time and response tendency have been verified using a prototype experiment. More importantly, based on the interplay between thermal effects and mechanical performances such as out-of-plane sensitivity, optimized design guidelines are proposed to reduce the thermally induced deformation as well as the rise time without compromising other performances. Vice versa, the guidelines can also help achieve higher performances

without the expense of more serious thermal effects. The analysis and design guidelines may pave the way for designing temperature-tolerant, high-performance optomechanical devices, which contain laser-induced heat sources and an elastic sensing structure with one sensitive axis, and that are not limited to optomechanical accelerometers.

Acknowledgment

The authors would like to thank the support from the National Natural Science Foundation of China (NSFC No. 60908025), the nanofabrication common platform of Suzhou Institute Nano-Tech and Nano-Bionics, Chinese Academy of Science.

ORCID iDs

Qianbo Lu  <https://orcid.org/0000-0003-4195-7602>

References

- [1] Krause A G, Winger M, Blasius T D, Lin Q and Painter O 2012 A high-resolution microchip optomechanical accelerometer *Nat. Photon.* **6** 768–72
- [2] Hall N A, Okandan M, Littrell R, Serkland D K, Keeler G A, Peterson K, Bicen B, Garcia C T and Degertekin F L 2008 Micromachined accelerometers with optical interferometric read-out and integrated electrostatic actuation *J. Microelectromech. Syst.* **17** 37–44
- [3] Loh N C, Schmidt M A and Manalis S R 2002 Sub-10 cm³ Interferometric accelerometer with nano-g resolution *J. Microelectromech. Syst.* **11** 182–7
- [4] Manalis S R, Minne S C, Atalar A and Quate C F 1996 Interdigital cantilevers for atomic force microscopy *Appl. Phys. Lett.* **69** 3944–6
- [5] Zhao S, Hou C, Zhang J, Bai J and Yang G 2012 A high-resolution displacement sensor based on a grating interferometer with the phase modulation technique *Meas. Sci. Technol.* **23** 105102–7
- [6] Ashkin A 1980 Applications of laser radiation pressure *Science* **210** 1081–8
- [7] Wang N, Yao B D, Chan Y F and Zhang X F 2003 Enhanced photothermal effect in Si nanowires *Nano Lett.* **3** 475–7
- [8] Srinivasan P and Spearing S M 2008 Effect of heat transfer on materials selection for bimaterial electrothermal actuators *J. Microelectromech. Syst.* **17** 653–67
- [9] Demirel K, Yazgan E, Şimşek D and Akın T 2016 A new temperature-tolerant RF MEMS switch structure design and fabrication for ka-band applications *J. Microelectromech. Syst.* **25** 60–8
- [10] Hopcroft M A, Nix W D and Kenny T W 2010 What is the Young's modulus of silicon *J. Microelectromech. Syst.* **19** 229–38
- [11] Brookshire K L, Rafiei R, Martyniuk M, Silva K, Faraone L and Liu Y 2016 Investigation of thermal expansion effects on Si-based MEMS structures *J. Microelectromech. Syst.* **25** 549–56
- [12] Daudersadt U A, Sarro P M and Middelhoek S 1997 Temperature dependence and drift of a thermal accelerometer *Proc. Transducers '97* pp 1209–12
- [13] Lakdawala H and Fedder G K 2004 Temperature stabilization of CMOS capacitive accelerometer *J. Microeng.* **14** 559–66

- [14] Tsai M H, Liu Y C, Liang K C and Fang W 2015 Monolithic CMOS-MEMS pure oxide tri-axis accelerometers for temperature stabilization and performance enhancement *J. Microelectromech. Syst.* **24** 1916–27
- [15] Zotov S A, Simon B R, Trusov A A and Shkel A M 2015 High quality factor resonant MEMS accelerometer with continuous thermal compensation *IEEE Sens. J.* **15** 5045–52
- [16] Comi C, Corigliano A, Langfelder G, Zega V and Zerbini S 2016 Sensitivity and temperature behavior of a novel z-axis differential resonant micro accelerometer *J. Micromech. Microeng.* **26** 035006
- [17] Zhang S, Jiang X, Lapsley M, Moses P and ShROUT T R 2010 Piezoelectric accelerometers for ultrahigh temperature application *Appl. Phys. Lett.* **96** 013506
- [18] Lee K, Takao H, Sawada K and Ishida M 2003 Low temperature dependence three-axis accelerometer for high temperature environments with temperature control of SOI piezoresistors *Sens. Actuators A* **104** 53–60
- [19] Fender A et al 2008 Two-axis temperature-insensitive accelerometer based on multicore fiber Bragg gratings *IEEE Sens. J.* **8** 1292–7
- [20] Dai G, Li M, He X, Du L, Shao B and Su W 2011 Thermal drift analysis using a multiphysics model of bulk silicon MEMS capacitive accelerometer *Sens. Actuators A* **172** 369–78
- [21] Acar C and Shkel A M 2003 Experimental evaluation and comparative analysis of commercial variable-capacitance MEMS accelerometers *J. Micromech. Microeng.* **13** 634
- [22] Furlong C and Pryputniewicz R J 2003 Optoelectronic characterization of shape and deformation of MEMS accelerometers used in transportation applications *Opt. Eng.* **42** 1223–31
- [23] Gagliardi G, Salza M, Ferraro P, Denatale P, Maio A D and Carlino S 2008 Design and test of a laser-based optical-fiber Bragg-grating accelerometer for seismic applications *Meas. Sci. Technol.* **19** 085306
- [24] Che W S and Oh J H 1996 Development of force-balance accelerometer with high accuracy for precision motion measurement *Meas. Sci. Technol.* **7** 1001–11
- [25] Dalola S, Ferrari V and Marioli D 2012 Micromachined piezoresistive inclinometer with oscillator-based integrated interface circuit and temperature readout *Meas. Sci. Technol.* **23** 035107
- [26] Lu Q, Bai J, Wang K and He S 2017 Design, optimization, and realization of a high-performance MOEMS accelerometer from a double-device-layer SOI wafer *J. Microelectromech. Syst.* **26** 859–69
- [27] Ashkin A 1970 Acceleration and trapping of particles by radiation pressure *Phys. Rev. Lett.* **24** 156–9
- [28] Krishnan R S 1979 *Thermal Expansion of Crystals* (Oxford: Pergamon)
- [29] Saleh B E A and Malvin C T 1991 *Fundamentals of Photonics* (New York: Wiley)
- [30] Weakliem H A and Redfield D 1979 Temperature dependence of the optical properties of silicon *J. Appl. Phys.* **50** 1491–3
- [31] Hall J J 1967 Electronic effects in the elastic constants of n-type silicon *Phys. Rev.* **161** 756–61
- [32] Hull R 1999 *Properties of Crystalline Silicon* (London: IET Publishing)
- [33] Glassbrenner C J and Slack G A 1964 Thermal conductivity of silicon and germanium from 3 k to the melting point *Phys. Rev.* **134** 634–6
- [34] Pisano A P and Cho Y H 1989 Mechanical design issues in laterally-driven microstructures *Proc. Transducers '89* pp 1060–4
- [35] Cho Y H and Pisano A P 1990 Optimum structural design of micromechanical crab-leg flexures with microfabrication constraints *Proc. ASME* pp 31–50
- [36] Lu Q, Wang C, Bai J, Wang K, Lou S, Jiao X, Han D, Yang G, Liu D and Yang Y 2016 Minimizing cross-axis sensitivity in grating-based optomechanical accelerometers *Opt. Express* **24** 9094–111
- [37] Zhang L, Lu J, Takagi H and Maeda R 2013 Analytical and experimental study on sensitivity of planar piezoresistive vibration sensor *Japan. J. Appl. Phys.* **52** 106502
- [38] Da Y T 1992 Thermal shock phenomena under high-rate response in solids *Annu. Rev. Heat Transfer* **4** 111–85
- [39] Tzou D Y 1992 Thermal resonance under frequency excitations *J. Heat Trans.* **114** 310–6
- [40] Srinivasan P 2012 Modeling the distribution of phonon density for designing high quality thermal resonators *Int. J. Heat Mass Transfer* **55** 5729–36
- [41] Kaminski W 1990 Hyperbolic heat conduction equation for materials with a nonhomogeneous inner structure *J. Heat Trans.* **112** 555–60
- [42] Salazar A 2006 Energy propagation of thermal waves *Eur. Phys. J.* **27** 1349
- [43] Lu Q, Wang C, Bai J, Wang K, Lian W, Lou S, Jiao X and Yang G 2015 Subnanometer resolution displacement sensor based on a grating interferometric cavity with intensity compensation and phase modulation *Appl. Opt.* **54** 4188–96